Mid-infrared N_2O absorption sensor for high-enthalpy flows relevant to hypersonic ground testing

Benjamin R. Steavenson*, Laura Munera*, Tristan Z. Crumley*, Denise Y. Guerra[†], Krystal Corral-Martinez[†], and Daniel I. Pineda[‡]

The University of Texas at San Antonio (UTSA), San Antonio, Texas, 78249, USA

In this paper we describe the development of a mid-infrared laser absorption spectroscopy sensing method for nitrous oxide (N_2O) concentration and temperature in high-enthalpy flows. This was accomplished by scanning the wavelength of narrowband laser light produced by a quantum cascade laser across multiple R-branch rovibrational transitions of N₂O near 4.42 µm and leveraging a Boltzmann regression of the population fractions. The Boltzmann regression method counteracts the otherwise poor-temperature sensitivity encountered when using two-line methods on these features, owing to relatively similar values of lower-state energy among the targeted transitions. Gas sensing of N₂O at low concentrations is of particular interest for high-enthalpy wind tunnel concepts wherein hypersonic flows of air are simulated via the decomposition of N_2O into the molecules nitrogen (N_2) and oxygen (O_2) . This measurement approach was demonstrated at the exit of a catalytic flow reactor through which mixtures of N₂O and N_2 were pre-heated and encouraged in thermal decomposition via a rhodium (Rh) / alumina catalyst bed. In this experimental configuration, an N₂O thermal decomposition reaction "light-off" temperature was identified and time-resolved measurements of N_2O mole fraction and temperature from light-off to near steady-state conditions were measured. Time-resolved thermochemistry measurements at 0.5 Hz are demonstrated to capture transient reactor phenomena that would otherwise be missed with sampling-based (e.g., gas chromatograph) methods, providing a promising avenue for real-time in-situ sensing in potential ground-testing systems producing high enthalpy air from N_2O .

I. Nomenclature

 α = absorbance

 ν = spectral frequency

P = pressure

X = species mole fraction

S = linestrength T = temperature L = path length A = absorption area

LAS = laser absorption spectroscopy

QCL = quantum cascade laser

II. Introduction

HIGH-ENTHALPY air flows greater than Mach 5 are relevant to both established and emerging hypersonic vehicle concepts, including for air-breathing scramjet-powered flight as well as Earth re-entry applications for both crewed and uncrewed aerospace vehicles. Ground-testing—a significant aspect of aerospace vehicle and propulsion system testing, evaluation, and qualification—faces unique challenges in the hypersonic regime, as the mass flow rate and power

^{*}Graduate Research Assistant, Dept. of Mechanical Engineering, 1 UTSA Circle, AIAA Student Member.

[†]Undergraduate Research Assistant, Dept. of Mechanical Engineering, 1 UTSA Circle, AIAA Student Member.

[‡]Assistant Professor, Dept. of Mechanical Engineering, 1 UTSA Circle, AIAA Member.

requirements are technically and economically substantial \blacksquare . High-Mach-number flows can be achieved by expansion of subsonic flow through nozzles in impulse facilities (e.g., Ludwieg tube $\blacksquare 2 - 4 \parallel$); however, the high flow velocities come at the expense of gas temperature, reducing the similarities between testing and flight conditions unless significant gas heating is employed, potentially requiring MW-scale power for high mass flow rates. Impulse facility heating can mitigate this difference, but material limitations (e.g., ~ 700 K for stainless steel driver tube) limit achievable enthalpies in the test section. Arcjets $\blacksquare 3 - 9 \parallel$ use plasma discharges to simultaneously accelerate and heat the test gas, but yield a partially-ionized and -dissociated gas composition which may affect material testing. For these reasons, researchers have explored concepts involving exothermic chemical reactions to efficiently and reliably increase the enthalpy of the test gases in ground test facilities, most notably using the exothermic decomposition of nitrous oxide (N₂O) into molecular nitrogen (N₂) and oxygen (O₂) to simulate high-enthalpy air $\blacksquare 0 - 12 \parallel$. Such concepts may require verification and/or validation that the test gas is in fact free of residual N₂O prior to further investment of implementation in hypersonic ground-testing facilities.

Nitrous oxide (N₂O) is a relatively accessible oxidizer that can be readily stored as a liquid owing to its high vapor pressure of 52 bar at ambient temperatures [13]. N_2O naturally exothermically decomposes into N_2 and O_2 at high temperatures (generally above 800 K); however, the temperature at which exothermic decomposition occurs can be brought down to those which are more economical for continuous process heating through the use of one or more solid catalysts $\boxed{14}$. Most available literature on N_2O decomposition through the use of a solid catalyst is related to the potential use of N₂O as a monopropellant for in-space propulsion applications [13, 15, 19], with publicly-available literature regarding specific application to simulating hypersonic high enthalpy flows more scarce [11] 16]. Commonly used catalysts for N₂O decomposition include iridium, ruthenium, rhodium, nickel, copper, and cobalt or one or more combinations of these. In general, the catalyst-based approach functions through the adsorption of N_2O molecules to active sites on the catalyst surface, which retains the oxygen and releases an N₂ molecule, after which the oxygen is released as O_2 (after merging with another oxygen from nearby active site) or attaches to another N_2O molecule 14. Few studies, if any, have assessed the conversion efficiency of this process using techniques other than gas-sampling based methods (e.g., gas chromatograph), which can potentially miss transient events and highly reactive (and undesirable) non-O₂ and non-N₂ products, such as nitric oxide (NO). To better characterize the performance and product selectivity of catalytic devices and processes which aim to decompose N₂O into high-enthalpy air for hypersonic ground testing—as well as enable more granular kinetic studies on the heterogeneous chemistry of existing and emerging catalysts used for this purpose—new in-situ diagnostics are required.

In this paper, we describe the development of a mid-infrared (mid-IR) laser absorption sensing concept which can detect N_2O species mole fraction in high-enthalpy flows as well as accurately measure associated gas temperatures. We first describe the theory of laser absorption spectroscopy (LAS) and Boltzmann regression underlying the sensing technique. We then detail our wavelength selection and experimental setup, including our reactor configuration. Finally, we demonstrate the sensing strategy with species mole fraction and temperature measurements made in a catalyst-assisted, thermally decomposing flow of N_2O mixed with N_2 .

III. Background

A. Laser absorption spectroscopy

Laser absorption spectroscopy (LAS) leverages the resonance of monochromatic collimated laser light energy with the discrete energy modes of gas molecules and atoms (arising from quantum mechanics) to discern thermochemical properties of flow fields using light absorption. Here, we briefly review the fundamentals of LAS to assist the reader with the measurements described in this paper. Lasers are specifically used as the radiation source in LAS measurements due to their monochromatic and collimated nature; additionally, lasers are often spectrally narrow and tunable in wavelength, allowing for high-resolution spectrally-resolved measurements of one or more features present in the absorption spectra of targeted gas species.

The Beer-Lambert law, shown in Eq. (1), describes the relationship between spectral and thermodynamic variables, as well as incident and transmitted laser light intensity I_0 and I_t . By integrating Eq. (1) with respect to frequency ν [cm⁻¹], absorbance area A [cm⁻¹] can be determined from spectrally-resolved absorbance $\alpha(\nu)$ [unitless], shown below in Eq. (2), being only a function of the thermophysical variables pressure P [atm], absorbing species mole fraction X, transition linestrength S(T) [cm⁻²/atm], and optical path-length L [cm] [20].

$$\alpha(\nu) = -\ln\left(\frac{I_t}{I_0}\right) = PXS(T)L\phi(\nu) \tag{1}$$

$$A = \int_{-\infty}^{\infty} \alpha(\nu) d\nu = PXS(T)L \tag{2}$$

To measure one or more spectral absorption features (in this work, rovibrational transitions), laser light is scanned across a range of wavelengths while passing through a test gas and into a photovoltaic detector, on which laser intensity is recorded. Upon absorption by a rovibrational transition, the transmitted laser light upon the detector is reduced. This is represented in Fig. \blacksquare wherein incident and transmitted laser intensity I as a function of time t is presented on the left and absorption as a function of ν is presented on the right.

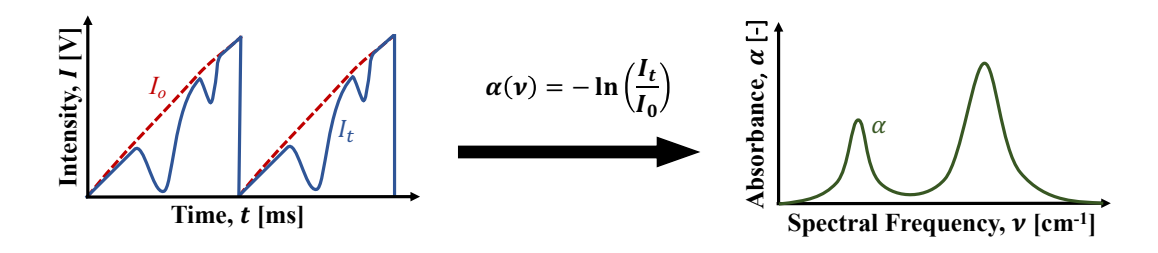


Fig. 1 Determination of absorbance from transmitted and incident laser light intensity from a scanned wavelength LAS measurement

To interpret the measured absorption data, a Voigt lineshape model (a convolution of a Gaussian and Lorentzian profile) can be fit to measured $\alpha(v)$ using non-linear regression [21]. After fitting, A can be numerically evaluated, assisting in the determination of thermodynamic state variables T and X as shown in Eq. [2] assuming that L is known from the experimental geometry and P is known independently. For multiple absorption features j, multiple A_j can be determined. The ratio of two absorption areas or integrated spectral absorption coefficients reduces to a ratio, R, of $S_j(T)$, being a function of T only, is shown in Eq. (3)

$$R = \frac{A_1}{A_2} = \frac{S_1(T)}{S_2(T)} = f(T) \tag{3}$$

Because $S_j(T)$ is a feature- or transition-specific spectral property, calculable from values readily available in the HITEMP and HITRAN databases [22] [23], it is possible to infer T with the simultaneous measurement of two or more spectral absorption features [24]. With T determined, $S_j(T)$ can be evaluated and X can be calculated using Eq. (20).

$$X = \frac{A_j}{PS_j(T)L} \tag{4}$$

B. Boltzmann regression

When multiple absorption features are simultaneously recorded (generally more than two), a *multi-line Boltzmann* regression can be used to determine temperature and species mole fraction [25]. The Boltzmann regression method counteracts the otherwise poor temperature sensitivity encountered when using traditional two-line methods with features whose values of lower-state energy are relatively similar, which typically leads to relatively poor temperature sensitivity [26]. Defining linestrength of a single spectral transition j, shown in Eq. (5), as a function of temperature, T, the partition function variation multiplied by a stimulated emission factor, $z(T, \bar{v_j})$, the lower state energy of the transition, E''_j , and a reference temperature usually taken at $T_0 = 296$ K [20] [23].

$$S_j(T) = S_j(T_0)z(T, \bar{v_j}) \left(\frac{T_0}{T}\right) \exp\left[-\frac{hcE_j''}{k_B} \left(\frac{1}{T} - \frac{1}{T_0}\right)\right]$$
 (5)

where the line strength evaluated at the reference temperature is noted as $S_j^0 = S_j(T_0)$ and $z(T, \bar{v_j})$, defined in Eq. (6), is a function of the partition function, $\mathcal{Z}(T)$, and the average wavenumber $\bar{v_j}$.

$$z(T, \bar{v_j}) \approx z(T) = \frac{Z(T_0)}{Z(T)} \cdot \frac{1 - \exp\left(-\frac{hc}{k_B T} \bar{v_j}\right)}{1 - \exp\left(-\frac{hc}{k_B T_0} \bar{v_j}\right)}$$
(6)

Per Minesi et al. [25], the average wavenumber $\bar{v_j}$ of the features used in the multi-line Boltzmann regression can be used, assuming that they are spectrally close, yielding an approximation of the simulated emission factor to within 0.1%. Taking the natural logarithm of Eq. (5):

$$\ln[S_j(T)] = \ln\left[S_j^0 z(T) \left(\frac{T_0}{T}\right)\right] - \frac{hc}{k_B} \left(\frac{1}{T} - \frac{1}{T_0}\right) E_j^{"} \tag{7}$$

Combining Eq. (2) with Eq. (7):

$$\ln\left[\frac{A_j}{PS_j^0L}\right] = \ln\left[Xz(T)\left(\frac{T_0}{T}\right)\right] + E_j''\left[\frac{hc}{k_B}\left(\frac{1}{T_0} - \frac{1}{T}\right)\right]$$
(8)

This linear relationship is a direct representation of the Boltzmann population density function [27]. Thus, $\frac{A_j}{PS_j^0L}$ is related to the degree with which the lower state of the transition j at temperature T is populated relative to the population at T_0 [25]. Eq. (8) is of the linear form y = ax + b, the linearization of which is shown in Fig. 2.

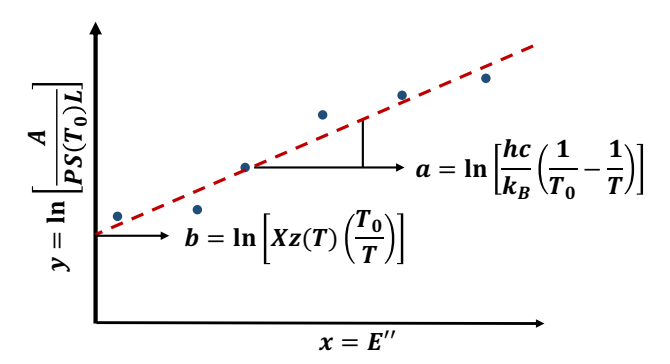


Fig. 2 Representative sketch of Boltzmann regression for a measurement spanning 6 spectral absorption features

Finally, temperature, T, and species mole fraction, X can be determined by re-arranging the linearized Eq. (8). In Eqs. (9) and (10), a represents the slope and b represents the y-intercept of the regression line.

$$T = \left[\frac{1}{T_0} - \frac{ak_B}{hc}\right]^{-1} \tag{9}$$

$$X = \frac{\exp(b)}{z(T)} \left(\frac{T}{T_0}\right) \tag{10}$$

IV. Method

A. Wavelength selection

To determine the appropriate spectral absorption features to target for this experiment, a spectral line survey was conducted between 2257 and 2265 cm⁻¹, in the v_3 fundamental bands of N_2O . This spectral frequency range is associated with the quantum cascade laser (QCL), centered at 4.42 μ m, used in this experiment. Fig. 3 shows the rovibrational spectral absorption lines (black) and features (red) for N_2O in this spectral frequency range. To the left, near 2259 cm⁻¹, an R-branch bandhead can be seen. Although these lines offer high contrast in lower state energy, they are not well isolated, leading to no nearby non-absorbing regions which are needed in scanned-wavelength methods to mitigate beam steering and thermal emission effects [28]. Due to this, spectral absorption lines located to the right of the bandhead were targeted in this experiment. Although these lines have high absorbance strength and are spectrally isolated from one another, they all have similar lower state energies. However, due to the large scan depth of the QCL used in this experiment at a scan rate of 2 kHz, 6 spectral absorption features (highlighted) were fully resolved and temperature and species mole fraction could be determined via Boltzmann regression.

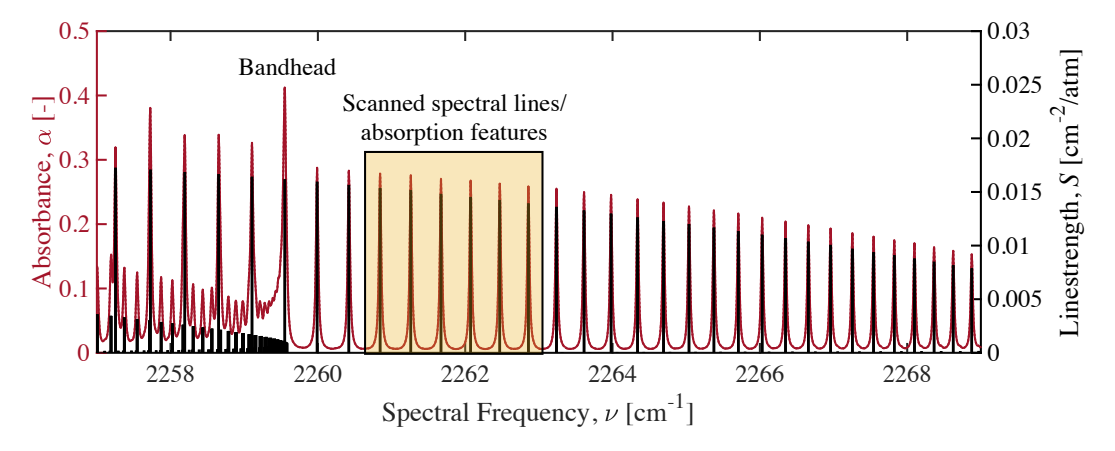


Fig. 3 Simulated spectral lines and absorption features for N₂O over the wavenumber range accessible with a 4.42 μ m conducted at: T = 2500 K, P = 1 atm, L = 1 cm, and $X_{N,O} = 0.25$.

B. Laser absorption spectroscopy setup

To obtain measurements of both N_2O mole fraction and temperature, a Quantum Cascade Laser (QCL, ALPES Lasers) was used as a light source whose beam was passed through a flow of Rhodium (Rh)/alumina catalyst-assisted, thermally decomposing N_2O . The laser beam was first passed through a flip-mounted germanium (Ge) etalon crystal, allowing for the conversion from the time to spectral frequency domain of the measured laser light intensity. The beam was then focused to the center of the flow using a pair of concave mirrors (f = 100 mm). Finally, the beam was passed through a focusing lens, iris (both increasing SNR), and spectral filter (limiting potential noise due to thermal radiation). Background and transmitted laser intensities were measured using a photovoltaic detector (Vigo Photonics) while the associated voltage data was collected at 80 Ms/s/channel using an external oscilloscope (PicoScope 4000 series). This resulted in 20 ms measurements during which both lasers were scanned 100 times. A schematic of the optical setup is shown in Fig. [4]

C. Catalytic reactor design and implementation

A student-designed and manufactured catalytic flow reactor was developed for this study, and consists of a 6-inch long stainless steel tube (OD 1.130 inches, ID 0.730 inches). 25 grams of Rhodium (Rh) on alumina pellet (32 mm in length) catalyst were contained within the reactor, occupying approximately 2.5 vertical inches and being held in place by an upper and lower stainless steel screen. Rhodium on alumina was chosen as a catalyst owing to its relative availability, cost, and previously demonstrated success (however modest) in the literature in thermally decomposing N_2O at low temperatures (500 K). Test gas enters through a compression fitting at the base of the reactor while a K-type

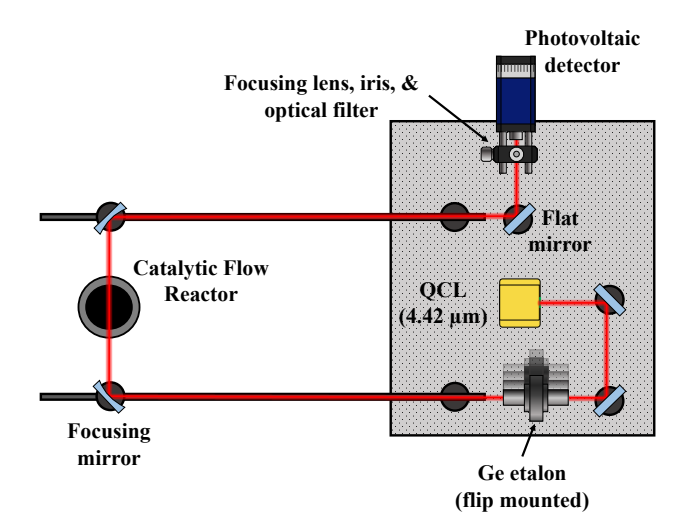


Fig. 4 Schematic of catalytic flow reactor and LAS measurement system

thermocouple is secured in a similar manner, measuring the temperature within but near the top of the catalyst bed. The reactor was fastened to an optical breadboard with a pair of optical posts. N_2O and N_2 were supplied to the reactor from the bottom, and their volumetric flow rates were controlled using 25- and 100-liter per minute (LPM) rotameters (Brooks Instruments), respectively. Finally, insulated heating tape (Brisk Heat) was used to heat the stainless steel hose carrying the reactants to the reactor as well as the reactor. A schematic of the reactor is shown in Fig. $\boxed{5}$.

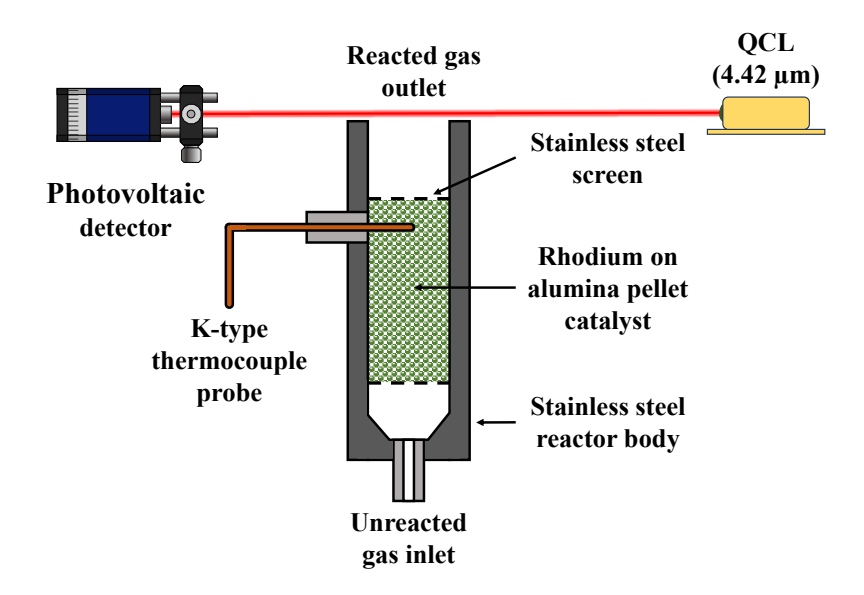


Fig. 5 Cross-section schematic of catalytic flow reactor

Because the rotameters used in this experiment were calibrated for air and not the test gases used (e.g., N_2O , N_2), a simplified correction factor was derived and applied to the recorded volumetric flow rates (neglecting near-wall effects of the rotameter float). Defining the volumetric flow rate \dot{V} as the mean cross-sectional area \bar{A} times the mean fluid velocity \bar{v} , a force balance in the z direction can be conducted, equating the weight and drag forces on the rotameter ball to each other.

$$mg = \frac{1}{2}C_D \rho_{\text{fluid}} \left(\frac{\dot{V}}{\bar{A}}\right)^2 \tag{11}$$

where C_D is the drag coefficient of the ball and ρ_{fluid} is the fluid density. Because the weight force is the same for two different fluids, and the same position on the variable-area rotameter corresponds to the same value of \bar{A} , the drag forces can be set equal to each other and Eq. (12) is derived, relating the volumetric flow rate of air to that of the actual gas flowing through the rotameter.

$$\dot{V}_{\rm gas} = \sqrt{\frac{\rho_{\rm air}}{\rho_{\rm gas}}} \cdot \dot{V}_{\rm air} \tag{12}$$

This correction factor is expected to have significant uncertainty owing to the neglect of near-wall effects of the rotameter float; however, the accuracy of the flow rates does not affect the diagnostic performance, which is the main focus of this study.

D. Experimental procedure

To demonstrate the diagnostic technique, two types of experiments were conducted using the catalyst flow reactor paired with the N_2O -sensitive QCL. The first type of experiment determined the temperature at which the inlet gas (N_2O and N_2) began thermally decomposing with the assistance of the catalyst (aka, the "light-off" temperature). The second type of experiment recorded time histories of the N_2O mole fraction and temperature at the exit of the reactor for a range of initial temperatures near the light-off temperature.

In the first experiment, mixtures of 31--33% N_2O and 69--67% N_2 by mass flow rate were pre-heated and fed into the reactor at temperatures ranging from 483 to 613 K (210 to 340° C) for a total of 12 independent reactor flow conditions. For this and the second experiment, it was assumed that the inlet gas temperature and catalyst bed temperature were equal. The temperature of the catalyst bed (measured with the thermocouple) was then monitored to see whether it remained constant or changed (indicating a chemical reaction). When the temperature reached near steady-state operation, an LAS measurement of N_2O mole fraction and temperature was performed at the exit of the reactor. This included a measurement of both the incident light intensity (colloquially called a *background* measurement in LAS practice) and the transmitted light intensity (with N_2O flow present), allowing Eq. (1) to be applied. Additionally, a residence time was calculated for each reaction by dividing the length of the catalyst bed by the unreacted N_2O velocity.

In the second experiment, mixtures of 33% N_2O and 67% N_2 by volume were pre-heated and fed into the reactor at initial catalyst temperatures of 572, 586, 596, 601, 605, 609 K (299, 313, 323, 328, 323, 336°C), all near the expected light-off temperature. Reactor exit N_2O mole fraction and temperature were measured every 2 seconds for 10 minutes using the previously discussed optical diagnostic technique, monitoring the progress of the catalytic decomposition of the N_2O . Additionally, the catalyst bed temperature was monitored using the embedded thermocouple.

V. Data analysis

To move from raw photovoltaic detector intensity data, recorded in volts, to temporally resolved N_2O mole fraction and temperature, a spectral fitting routine—detailed and discussed in this section—was utilized. Specifically, this includes 1) the averaging, alignment and scaling of raw intensity data, 2) calculating absorbance using the Beer-Lambert law, 3) implementing a multi-line, non-linear spectral fitting routine, and 4) determining species mole fraction and temperature via multi-line Boltzmann regression. These steps were conducted for all LAS measurements made in the first and second experiments, and was completed numerically using Matlab.

A. Spectral fitting

Following the collection of intensity data, the 100 laser scans collected per measurement were averaged, increasing signal-to-noise ratio (SNR). Cross correlation was then used to align all incident and transmitted intensity measurements, which had originally been performed asynchronously. With the transmitted and intensity signals aligned (See the left of Fig. 6), incident intensity signal scaling was conducted for all measurements, allowing for effects such as beam steering to be mitigated [?]. To accomplish this, an iterative approach to scaling was used where each incident intensity waveform was scaled incrementally until it matched the experimental data in a non-absorbing region, located between spectral features, of the signal as determined via spectral simulations using data from the HITEMP databases. Finally, the Beer-Lambert law was applied to all measurements, resulting in spectral absorbance as a function of time, as shown

in Fig. 6. Using a single intensity measurement recorded with a 2-inch germanium (Ge) etalon (Del Mar Photonics) placed in the beam path of the laser, a fifth-order polynomial relating the spectral frequency domain to time domain was derived. Because the relationship between time and spectral frequency is only a function of the laser settings (e.g., injection current, and operating temperature), this only has to be completed once per experiment. This polynomial was then used to convert spectral absorbance represented in the time domain to the spectral frequency domain in units of cm⁻¹), an example of which is shown in Fig. 6. It should be noted that this spectral frequency is relative to the measurement and not absolute; commonly, it is referred to as relative wavenumber.

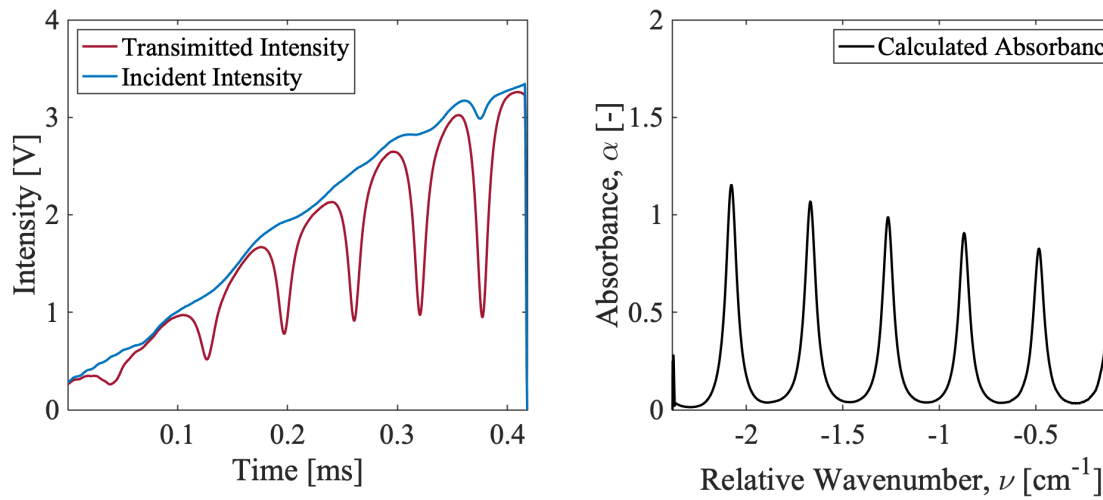


Fig. 6 Representative transmitted and incident laser intensity for N₂O as recorded by the detector (left) and calculated absorbance for N₂O (right)

To determine absorption area A_i , the measured spectral absorbance of each rovibrational transition must first be fit to a spectral lineshape model. The Voigt lineshape model—a convolution of the Gaussian and Lorentzian distributions representing the effects of Doppler and collisional broadening respectively [20]—is assumed in this study to adequately describe the lineshape of the recorded rovibrational transitions. A non-linear regression approach was utilized in MATLAB to fit Voigt lineshape models to all spectral absorption features. In this approach, three physical parameters were modeled for each spectral absorption feature j: linecenter $v_{0,j}$, collisional width $\Delta v_{C,j}$, and absorption area A_j . In order to constrain the fitting routine, the linecenter parameters for features (from lowest to highest wavenumber, or left to right in the right of Fig. (6) 1, 2, 3, 5, and 6 were fixed relative to feature 4, while feature 4 was allowed to vary independently. Additionally, the rovibrational transitions possessed similar enough broadening parameters to perform additional simplifications to increase the robustness of the multi-line fit. The collisional width Δv_C is given by Ω

$$\Delta v_{C,j} = P \sum_{Y} X_Y \cdot 2\gamma_{Y,j}(T) \tag{13}$$

-1.5

Calculated Absorbance

where $\gamma_{Y,j}(T)$ is the temperature-dependent collisional broadening coefficient for N₂O transition j and collision partner Y, X_Y is the mole fraction of collision partner Y, and the expression is summed over all of the collision partners present in the gas mixture. The temperature-dependence is captured by:

$$2\gamma(T) = 2\gamma_{Y,j}(T_0) \left(\frac{T_0}{T}\right)^N \tag{14}$$

where $\gamma_{Y,j}(T_0)$ is the reference temperature collisional broadening coefficient for N₂O transition j and collision partner Y, and N is the temperature-dependent exponent. $\gamma_{Y,j}(T_0)$ and N are tabulated in the HITRAN and HITEMP database assuming air as the collision partner for many transitions, including those of N_2O investigated here. By floating $\Delta v_{C,i}$ in the spectral fitting routine, the gas composition and temperature need not be known in advance to obtain A_i and subsquently T and $X_{N,O}$ as described in Section III. Fortuitously, N values for all targeted transitions in this work are the same for $2\gamma_{N,O-air}$, and Eq. (14) can be simplified to Eq. (15), wherein the collisional width of feature A is equal to the collisional width of feature B times the ratio of the collisional broadening coefficients:

$$\Delta \nu_{C,A} = \Delta \nu_{C,B} \left(\frac{\gamma_{N_2O-air,A}}{\gamma_{N_2O-air,B}} \right)$$
 (15)

A full discussion of collisional width can be found in $\square 0$. Using this relationship the collisional widths of features 1, 2, 3, 5, and 6 were fixed while the collisional width of feature 4 was floated. This procedure assumes that the all values of $\gamma_{Y,j}(T_0)$ are affected equally by all collision partners Y in the gas. In fitting both the linecenter and collisional width, spectral feature four was selected as the floating parameter due to its separation from the beginning/end of the scan as well as its isolation from an ambient CO_2 feature present near some of the stronger features in the scan. Additionally, the absorption areas for each feature were also floated, leading to a total of 8 floated parameters and 10 fixed parameters. With the fitting routine complete, the normalized residual with respect to the measured data was determined. An example of the measured, spectrally fitted, and residual data is presented in Fig. \square The residuals are all below 5%, indicating the appropriateness of the Voigt lineshape model for these features.

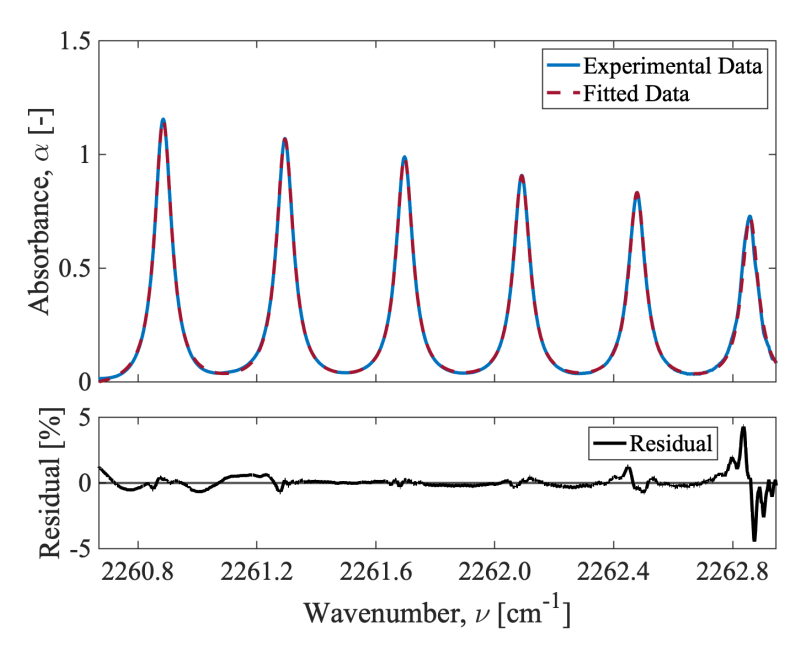


Fig. 7 Representative experimentally determined (blue) and spectrally Voigt-fit (red) absorbance for N_2O (top) and percent residual between experimental and fitted absorbance (bottom)

B. Thermochemical analysis

With absorbance areas A_j determined for all six spectral absorption features j, Boltzmann regression was used to determine species mole fraction and temperature, being temporally resolved for the second (transient) experimental measurement. To accomplish this, each value for A_j was linearized using Eq. (8), where $y = \ln\left[\frac{A_j}{PS_j^0L}\right]$ and $x = E_j''$. This was then plotted and linearly fit with fitting coefficients $a = \frac{hc}{kB}\left(\frac{1}{T_0} - \frac{1}{T(r)}\right)$ and $b = \ln\left[X(r)q(T(r))\left(\frac{T_0}{T(r)}\right)\right]$. An example of this for N₂O is presented in Fig. 8. Here, the vertical error bars reflect a 95% confidence interval associated with the linear regression [29]. Additionally, because uncertainty of the lower state energy is reported as $\frac{\delta E''}{E''} \leq 10^{-6}$, its contributions were neglected and horizontal error bars were not plotted.

VI. Results and uncertainty

Presented below are the results from both the first experiments at steady state (determination of the light-off temperature) and second transient experiments (N_2O mole fraction and temperature time histories). Additionally, an

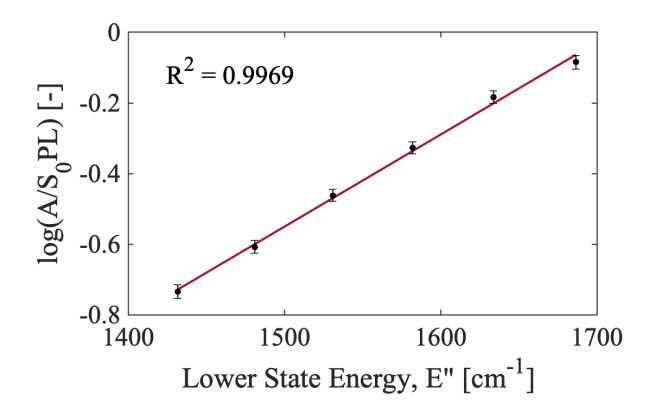


Fig. 8 Representative Boltzmann regression used to determine the linear regression coefficients a and b

uncertainty analysis associated with this LAS measurement technique is discussed. In both cases, Boltzmann regression coefficients a were used with Eqs. (9) (10) to determine temperature while Eq. 20 was used to determine N_2O mole fraction.

A. Results

Presented in Fig. Pare the initial and final conditions recorded in the first experiment type (steady state determination of light-off temperature). For all test conditions, the unreacted N_2O mole fraction values were between X = 0.266 and X = 0.288, reactant flow rate were between $\dot{m} = 0.313$ and $\dot{m} = 0.325$ g/s, and residence times between 0.116 and 0.113 s. It was observed that exit temperatures measured via LAS were lower than those measured via the thermocouple inside of the catalyst bed. As with the thermocouple measurements, the LAS-measured temperature indicated that the light-off point corresponded to a initial catalyst temperature at or above 600 K. LAS-measured N_2O mole fraction values recorded at the reactor exit trended down with increasing initial catalyst bed temperature. This result indicated that catalyst-assisted thermal decomposition was increasing with temperature.

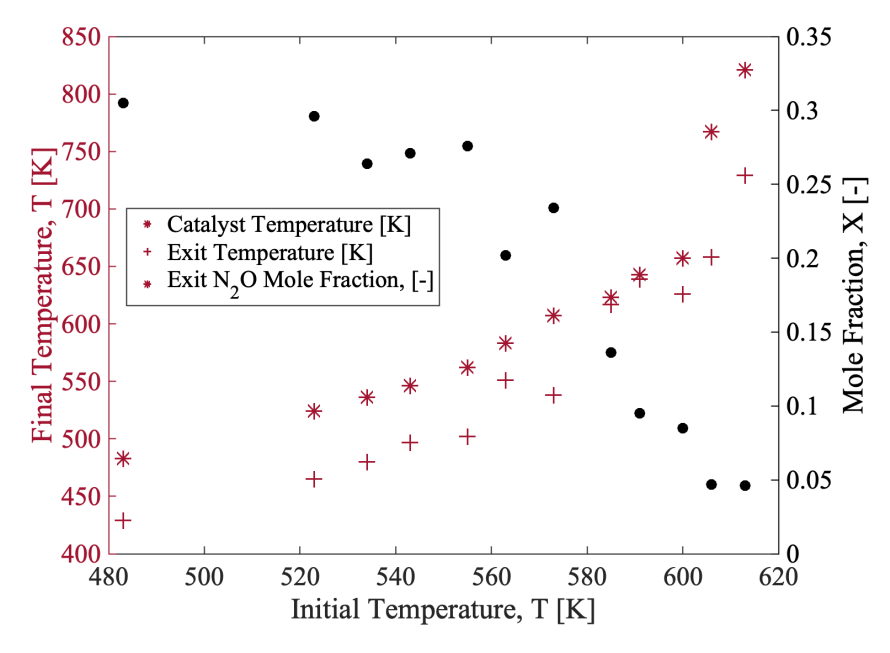
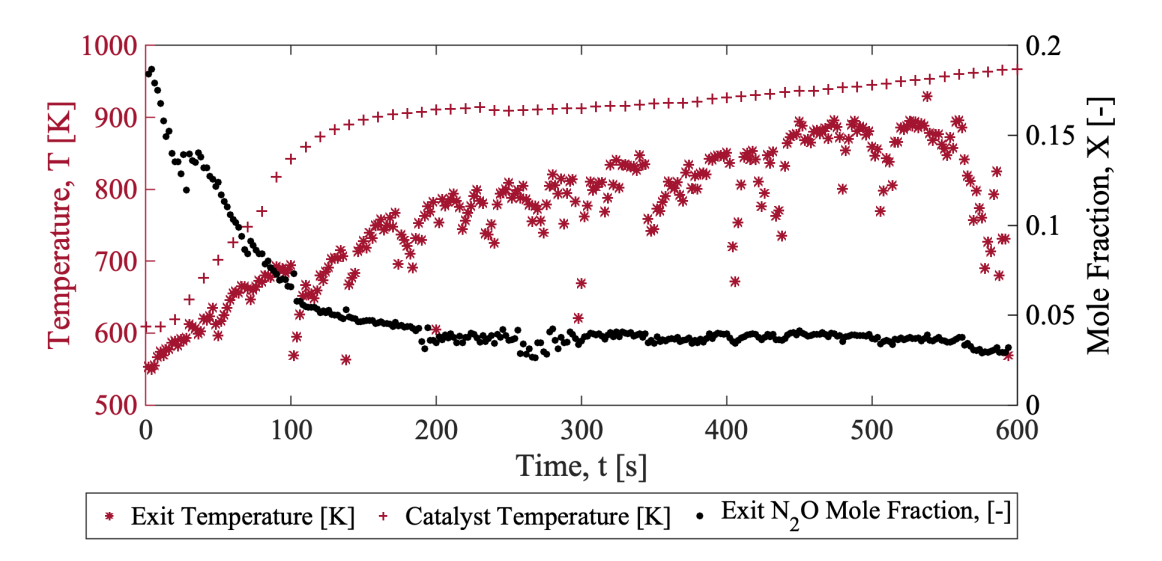


Fig. 9 Near steady-state catalyst bed and exit plane temperature (red) and exit plane N_2O mole fraction (black) over a range of initial catalyst bed temperatures.

Presented in Fig. $\boxed{10}$ are the LAS-measured reactor exit temperature and N_2O mole fraction alongside thermocouple-measured catalyst bed temperature for the reactor time-history measurement. A total of four transient cases were performed with the experimental configuration described in this paper; a representative example is shown here. The initial temperature of the catalyst bed was 609 K while the mass flow rates of $\dot{m}=0.126$ and $\dot{m}=0.199$ g/s for N_2O and N_2 respectively, equating to an inlet N_2O mole fraction of X=0.288. The experiment was recorded for a total of 10 minutes (600 seconds).



 $Fig. 10 \quad Reactor\ exit\ temperature\ and\ catalyst\ bed\ temperature\ (red)\ and\ N_2O\ mole\ fraction\ (black)\ measurements\ from\ a\ 10\ minute\ catalyst\ assisted\ N_2O\ thermal\ decomposition\ experiment\ with\ an\ initial\ temperature\ of\ 607\ K$

In the case of the catalyst bed temperature, it rapidly increased over the initial 150 seconds before increasing slowly for the remainder of the experiment. Likewise, the exit plane N_2O mole fraction decreased rapidly before plateauing for the remainder of the experiment. In the case of the exit plane temperature, it increased throughout the entire experiment, although this rate appeared to decrease. It was also observed that the exit temperature was less than that of the catalyst bed, although these temperatures converged as time passed. Finally, temperature transient events were observed throughout the entire time-resolved LAS measurement. It was also observed that these transient events generally increased in magnitude as the experiment proceeded.

B. Uncertainty analysis

In this section, the temperature and species mole fraction measurement uncertainties are derived with respect the the Boltzmann fitting parameter a, and its associated 95% confidence intervals as well as spectroscopic parameters of a given spectral absorption feature set, the experimental noise and reactor design parameters.

The uncertainty of function f, as a function of variables x_i , can be calculated using a Taylor expansion, shown in Eq. (16), assuming the measured variables, x_i , and measured variable uncertainties, δx_i , are independent from one another (30). Using this, the uncertainty of function f can be expressed as a function of its partial derivatives and independent variable uncertainties, shown in Eq. (17).

$$df(x_1, x_2, \dots) = \frac{\partial f}{\partial x_1} dx_1 + \frac{\partial f}{\partial x_2} dx_2 + \dots$$
 (16)

$$(\delta f)^2 = \left(\frac{\partial f}{\partial x_1} \delta x_1\right)^2 + \left(\frac{\partial f}{\partial x_2} \delta x_2\right)^2 + \dots$$
 (17)

Restating the equation for temperature:

$$T = \left[\frac{1}{T_0} - \frac{ak_B}{hc}\right]^{-1} \tag{18}$$

where T_0 , k_B , h, and c are constants and a is the slope of the Boltzmann regression. Applying Eq. (17) to Eq. (18) and accounting for uncertainty propagation [29]:

$$\frac{\delta T}{T} = \frac{k_B}{hc} T \delta a \tag{19}$$

where δa is the uncertainty in the slope of the Boltzmann regression, in this case evaluated as the 95% confidence interval associated with the linear fit.

Restating the equation for species mole fraction:

$$X = \frac{A_j}{PS_j(T)L} \tag{20}$$

where A_j , is the spectrally fit absorption area, P is the pressure, $S_j(T)$ is the linestrength, and L is the pathlength. Applying Eq. [17] to Eq. (20):

$$\frac{\delta X}{X} = \sqrt{\left(\frac{\delta A}{A}\right)^2 + \left(\frac{\delta S_j}{S_j(T)}\right)^2 + \left(\frac{\delta L}{L}\right)^2} \tag{21}$$

where δA is the absorbance area uncertainty defined as the mean residual of the spectral fit, δS_j is the linestrength uncertainty obtained from the HITRAN database, and δL is the pathlength uncertainty, taken to be the uncertainty associated with the machining of the reactor. It should be noted that the uncertainty associated with pressure was neglected as all experiments were preformed at standard atmospheric conditions (P = 1 atm).

Applying Eq. $\boxed{19}$ and $\boxed{21}$ to a typical LAS measured, reactor exit plane temperature and N₂O mole fraction, a relative temperature uncertainty of 9% was determined as well as a relative species mole fraction uncertainty of 6%.

VII. Conclusion and future work

In this work, a non-invasive, laser absorption-based N_2O mole fraction and temperature sensing method for highenthalpy reacting flows—with applications in real-time in-situ sensing in potential ground-testing systems producing high enthalpy air from N_2O —was developed and demonstrated at the exit plane of a catalytic flow reactor. In the demonstration, both high temperatures (> 900 K) and low species mole fractions (< 0.05) were measured, with relative uncertainties of 6% and 9% respectively, at a 0.5 Hz sample rate. This sample rate demonstrated that transient reactor phenomena, that may otherwise be missed with sampling-based (e.g., gas chromatograph) methods, were observable using the LAS method developed.

From the first set of experiments, a light-off temperature of $\geq 600~\mathrm{K}$ was observed for the reactor flow rates, Rh catalyst, and reactor geometry used in this study. This result was leveraged in selecting an appropriate initial catalyst bed temperature for the time-resolved measurements of catalyst bed temperature and reactor exit plane N_2O mole fraction and temperature. The results from the light-off temperature experiments as well as the time-resolved measurement indicate that the exit temperature was lower than the catalyst bed temperature. This is likely due to the thermocouple being located in the middle of the catalyst bed and additional thermal decomposition and/or heat transfer/loss taking place between the two measurement points, but future work will directly compare thermocouple measurements and LAS measurements at the same point in the flow to confirm this. Additionally, it was observed that during the time-resolved measurement, temperature (catalyst bed and exit plane) and N_2O mole fraction increased and decreased respectively, trending toward a steady-state value.

During the time-resolved measurement, transient temperature events were observed where exit plane temperature would drop briefly before returning to its trending value. However, this phenomenon was not observed in the catalyst bed temperature measurements and is likely due to the relatively low sample rate of the measurement (0.1 Hz) and thermocouple response time (0.5 s). Although the reason for these transient events is not hypothesized here, their measurement demonstrates the LAS sensing method's ability to measure relatively high-frequency transient reactor phenomena.

Moving forward, the authors plan to 1) redesign the catalyst flow reactor to include optical access via a pair of sapphire windows located directly above the catalyst bed and 2) add a nitric oxide (NO)-sensitive interband cascade

laser (ICL) to the optical setup [21]. The first will mitigate the effects of potential buoyancy-driven eddies located at the exit of the reactor due to N_2O having a higher density than air as well as any heat loss between the top of the catalyst bed and the exit of the reactor. The second will provide the ability to measure an unwanted NO decomposition intermediate species and help to verify that the exit gas is composed of N_2 and O_2 , both of which are not readily measurable by LAS in the mid-IR. With these changes, the authors hope to further develop this sensing method for its potential use in ground-testing facilities.

Acknowledgments

BRS and LM are supported by the American Chemical Society Petroleum Research Fund (ACS-PRF Grant No. 65560-DNI6). DYG gratefully acknowledges support from the UTSA McNair Scholars Program. KCM is supported by NSF Award No. 2135789.

The authors gratefully acknowledge the assistance of Haven Russell and Mr. David Kuenstler for their efforts in manufacturing the stainless steel reactor tube. The authors also thank Fabio A. Bendana, Chuyu Wei, Anil P. Nair, and Nicholas M. Kuenning for helpful discussions on signal processing methods during this project.

References

- [1] Anderson, J. D., *Hypersonic and High-Temperature Gas Dynamics*, 3rd ed., American Institute of Aeronautics and Astronautics (AIAA), Reston, VA, 2019. https://doi.org/10.2514/4.105142.
- [2] Anderson, J. D., Modern Compressible Flow, A Historical Perspective, 3rd ed., McGraw-Hill, New York, NY, 2002.
- [3] Hoffman, E. N., Lalonde, E. J., Garcia, M., Valeria Delgado, E., Chen, I., Bilbo, H. A., and Combs, C. S., "Characterization of the UTSA Mach 7 Ludwieg Tube," AIAA Science and Technology Forum and Exposition, AIAA SciTech Forum 2022, 2022, pp. 1–19. https://doi.org/10.2514/6.2022-1600.
- [4] Bashor, I. P., Hoffman, E., Gonzalez, G., and Combs, C. S., "Design and preliminary calibration of the utsa mach 7 hypersonic ludwieg tube," *AIAA Aviation 2019 Forum*, No. June, 2019, pp. 1–17. https://doi.org/10.2514/6.2019-2859.
- [5] Ground, C., Maddalena, L., Viti, V., and Hampshire, N., "1 . 6 MW Arc Heated Wind Tunnel Facility," 51st AIAA Aerospace Sciences Meeting, , No. January, 2013, pp. 1–15.
- [6] Wayne Guy, R., Clayton Rogers, R., Fuster, R. L., Rock, K. E., and Diskin, G. S., "The NASA langley scramjet test complex," 32nd Joint Propulsion Conference and Exhibit, No. July, 1996. https://doi.org/10.2514/6.1996-3243
- [7] Nations, M., Chang, L. S., Jeffries, J. B., Hanson, R. K., MacDonald, M. E., Nawaz, A., Taunk, J. S., Gökçen, T., and Raiche, G., "Characterization of a large-scale arcjet facility using tunable diode laser absorption spectroscopy," *AIAA Journal*, Vol. 55, No. 11, 2017, pp. 3757–3766. https://doi.org/10.2514/1.J056011
- [8] Baccarella, D., and Samuels, K. E., "Testing and Characterization of the University of Tennessee High-Enthalpy Tunnel," *AIAA Scitech 2023 Forum*, No. January, 2023, pp. 1–13. https://doi.org/10.2514/6.2023-1456
- [9] Raybon, I., Viganò, D., Maddalena, L., and Llc, A. A., "Measurement of Skin Friction in the University of Texas at Arlington Arcjet," *Journal of Spacecraft and Rocket*, 2023, pp. 1–9. https://doi.org/10.2514/1.A35615
- [10] Cawthra, J., and Eisenstadt, M., "Summary of Nitrous Oxide Investigations," Tr-75-231, , No. July, 1974, pp. 10-16.
- [11] Nicholson, J. R., Fishburne, E., and Edse, R., "An experimental investigation of the use of nitrous oxide in hypersonic wind tunnel testing facilities," Tech. Rep. ARL 66-0011, Office of Aerospace Research, United States Air Force, Columbus, OH, 1966.
- [12] Buttsworth, D. R., "Nitrous Oxide Decomposition for Supersonic Combustion Experiments in the USQ Ludwieg Tube Facility," *Proceedings of the Australian Combustion Symposium*, 2009, pp. 2–5.
- [13] Zakirov, V., Sweeting, M., Lawrence, T., and Sellers, J., "Nitrous oxide as a rocket propellant," *Acta Astronautica*, Vol. 48, No. 5-12, 2001, pp. 353–362. https://doi.org/10.1016/S0094-5765(01)00047-9.
- [14] Zakirov, V., Richardson, G., Sweeting, M., and Lawrence, T., "Surrey research update on N2O catalytic ecomposition for space applications," 37th Joint Propulsion Conference and Exhibit, No. July, 2001. https://doi.org/10.2514/6.2001-3922.

- [15] Lohner, K., Dyer, J., Doran, E., Dunn, Z., Krieger, B., Decker, V., Wooley, E., Sadhwani, A., Cantwell, B., and Kenny, T., "Design and development of a sub-scale nitrous oxide monopropellant gas generator," *Collection of Technical Papers 43rd AIAA/ASME/SAE/ASEE Joint Propulsion Conference*, Vol. 5, No. July, 2007, pp. 4417–4426. https://doi.org/10.2514/6.2007-5463.
- [16] Wickham, D., Hitch, B., and Logsdon, B., "Development and Testing of a High Temperature N2O Decomposition Catalyst," 46th AIAA/ASME/SAE/ASEE Joint Propulsion Conference & Exhibit, American Institute of Aeronautics and Astronautics, Reston, Virigina, 2010, pp. 1–14. https://doi.org/10.2514/6.2010-7128, URL http://arc.aiaa.org/doi/abs/10.2514/6.2010-7128
- [17] Hennemann, L., de Andrade, J. C., and de Souza Costa, F., "Experimental investigation of a monopropellant thruster using nitrous oxide," *Journal of Aerospace Technology and Management*, Vol. 6, No. 4, 2014, pp. 363–372. https://doi.org/10.5028/jatm.v6i4.382.
- [18] Saripalli, P. S., and Sedwick, R. J., "Nitrous oxide decomposition using inductively heated heat exchangers," *Journal of Propulsion and Power*, Vol. 36, No. 6, 2020, pp. 887–900. https://doi.org/10.2514/1.B37793
- [19] Di Martino, G. D., Gallo, G., Mungiguerra, S., Festa, G., and Savino, R., "Design and testing of a monopropellant thruster based on N2O decomposition in Pd/Al2O3 pellets catalytic bed," *Acta Astronautica*, Vol. 180, No. December 2020, 2021, pp. 460–469. https://doi.org/10.1016/j.actaastro.2020.12.016, URL https://doi.org/10.1016/j.actaastro.2020.12.016.
- [20] Hanson, R. K., Spearrin, R. M., and Goldenstein, C. S., Spectroscopy and optical diagnostics for gases, 1st ed., Springer, London, UK, 2016. https://doi.org/10.1007/9783319232522.
- [21] Steavenson, B., Hernandez-McCloskey, J., and Pineda, D. I., "Thermodynamic analysis of nitric oxide in an optically accessible, temperature-controlled gas cell via laser absorption spectroscopy," *AIAA Scitech 2023 Forum Forum*, No. January, 2023, pp. 1–11. https://doi.org/10.2514/6.2023-0011.
- [22] Rothman, L. S., Gordon, I. E., Barber, R. J., Dothe, H., Gamache, R. R., Goldman, A., Perevalov, V. I., Tashkun, S. A., and Tennyson, J., "HITEMP, the high-temperature molecular spectroscopic database," *Journal of Quantitative Spectroscopy and Radiative Transfer*, Vol. 111, No. 15, 2010, pp. 2139–2150. https://doi.org/10.1016/j.jqsrt.2010.05.001, URL http://dx.doi.org/10.1016/j.jqsrt.2010.05.001
- [23] Gordon, I., Rothman, L., Hargreaves, R., Hashemi, R., Karlovets, E., Skinner, F., Conway, E., Hill, C., Kochanov, R., Tan, Y., Wcisło, P., Finenko, A., Nelson, K., Bernath, P., Birk, M., Boudon, V., Campargue, A., Chance, K., Coustenis, A., Drouin, B., Flaud, J., Gamache, R., Hodges, J., Jacquemart, D., Mlawer, E., Nikitin, A., Perevalov, V., Rotger, M., Tennyson, J., Toon, G., Tran, H., Tyuterev, V., Adkins, E., Baker, A., Barbe, A., Canè, E., Császár, A., Dudaryonok, A., Egorov, O., Fleisher, A., Fleurbaey, H., Foltynowicz, A., Furtenbacher, T., Harrison, J., Hartmann, J., Horneman, V., Huang, X., Karman, T., Karns, J., Kassi, S., Kleiner, I., Kofman, V., Kwabia–Tchana, F., Lavrentieva, N., Lee, T., Long, D., Lukashevskaya, A., Lyulin, O., Makhnev, V., Matt, W., Massie, S., Melosso, M., Mikhailenko, S., Mondelain, D., Müller, H., Naumenko, O., Perrin, A., Polyansky, O., Raddaoui, E., Raston, P., Reed, Z., Rey, M., Richard, C., Tóbiás, R., Sadiek, I., Schwenke, D., Starikova, E., Sung, K., Tamassia, F., Tashkun, S., Vander Auwera, J., Vasilenko, I., Vigasin, A., Villanueva, G., Vispoel, B., Wagner, G., Yachmenev, A., and Yurchenko, S., "The HITRAN2020 molecular spectroscopic database," *Journal of Quantitative Spectroscopy and Radiative Transfer*, Vol. 277, 2022, p. 107949. https://doi.org/10.1016/j.jqsrt.2021.107949.
- [24] Girard, J. J., Spearrin, R. M., Goldenstein, C. S., and Hanson, R. K., "Compact optical probe for flame temperature and carbon dioxide using interband cascade laser absorption near 4.2µm," *Combustion and Flame*, Vol. 178, 2017, pp. 158–167. https://doi.org/10.1016/j.combustflame.2017.01.007, URL http://dx.doi.org/10.1016/j.combustflame.2017.01.007
- [25] Minesi, N. Q., Richmond, M. O., Jelloian, C. C., Kuenning, N. M., Nair, A. P., and Spearrin, R. M., "Multi-line Boltzmann regression for near-electronvolt temperature and CO sensing via MHz-rate infrared laser absorption spectroscopy," *Applied Physics B: Lasers and Optics*, Vol. 128, No. 12, 2022, pp. 1–17. https://doi.org/10.1007/s00340-022-07931-7. URL https://doi.org/10.1007/s00340-022-07931-7.
- [26] Zhou, X., Jeffries, J. B., and Hanson, R. K., "Development of a fast temperature sensor for combustion gases using a single tunable diode laser," *Applied Physics B: Lasers and Optics*, Vol. 81, No. 5, 2005, pp. 711–722. https://doi.org/10.1007/s00340-005-1934-y.
- [27] Pathria, R., and Beale, P., Statistical mechanics, 4th ed., Elsevier, London, UK, 2022.
- [28] Nair, A. P., Lee, D. D., Pineda, D. I., Spearrin, R. M., Kriesel, J., Hargus, W. A., Bennewitz, J. W., and Danczyk, S. A., "Mhz mid-infrared laser absorption of co and co2 for pressure, temperature, and species in rotating detonation rocket flows," *AIAA Propulsion and Energy 2020 Forum*, 2020, pp. 1–15. https://doi.org/10.2514/6.2020-3867

- [29] York, D., Evensen, N. M., Martinez, M. L., and De Basabe Delgado, J., "Unified equations for the slope, intercept, and standard errors of the best straight line," *American Journal of Physics*, Vol. 72, No. 3, 2004, pp. 367–375. https://doi.org/10.1119/1.1632486.
- [30] Chapra, S., and Canale, R., Numerical Methods for Engineers, 7th ed., November, McGraw-Hill, New York, NY, 2015.